Journal of Superconductivity and Novel Magnetism (2025) 38:59
https://doi.org/10.1007/s10948-024-06898-0

RESEARCH

Investigating the Structural, Electronic, Magnetic, Mechanical, Anisotropic and Optical Aspects of CoFeYSb (Y = V and Ti) Quaternary Heusler Alloys from First Principles

I. Bensehil[1,2] · H. Baaziz[3,4] · T. Ghellab[3,4] · F. Djeghloul[2,5] · S. Zaiou[2,6] · A. Kolli[2] · N. Guechi[2,7] · Z. Charifi[3,4]

Received: 17 July 2024 / Accepted: 27 December 2024

Abstract
This study employs first-principles calculations to explore the structural, elastic, electronic, magnetic, and optical properties of the quaternary Heusler compounds CoFeYSb (Y = V, Ti). The structural analysis confirms that both compounds are most stable in the YI configuration. CoFeVSb is found to exhibit ferromagnetic behavior, while CoFeTiSb shows ferrimagnetism. Elastic constants, cohesion energy, and formation energy calculations further validate the stability of the magnetic (I) phase for both materials. Band structure analysis reveals that these compounds are half-metallic, achieving 100% spin polarization at the Fermi level, with spin-down energy gaps of 0.55 eV for CoFeVSb and 0.61 eV for CoFeTiSb. The total magnetic moments comply with the Slater-Pauling 24-electron rule, with values of 3 μB for CoFeVSb and 2 μB for CoFeTiSb. Optical investigations, including the dielectric function, absorption coefficient, and energy loss function, demonstrate strong absorption in the visible and ultraviolet ranges. These results highlight the potential of CoFeYSb compounds for advanced optoelectronic and spintronic applications, offering new opportunities for their integration into electronic and photonic technologies.

Keywords Half-metallicity · Optical response · Spintronic devices · Optoelectronics

1 Introduction

Spintronic devices have emerged as promising candidates for future electronics, harnessing the magnetic moment (or spin) of electrons to enable advanced functionalities [1]. A pivotal advancement in electronic applications involves half metals [2], which demonstrate metallic conductivity in one spin channel while the other spin channel behaves as a semiconductor or insulator. These materials achieve 100% spin polarization due to a distinct divergence from the Fermi level, making these alloys excellent candidates for spintronic applications [3–5].

The pioneering work by de Groot and colleagues [6, 7] in 1983 marked the first prediction of half-metallic ferromagnetism in the NiMnSb Heusler alloy. This breakthrough sparked considerable interest and subsequent research into new classes of materials capable of exhibiting half-metallic properties. These advancements not only broaden our understanding of fundamental electronic structures but also pave the way for innovative spintronic applications in areas such as data storage, magnetic sensors, and quantum computing.

Heusler alloys are well-known for their remarkable ability to exhibit unique electronic and magnetic properties, including half-metallicity and semiferromagnetism. These materials are classified into two main families based on their chemical compositions and crystal structures: half-Heusler and full-Heusler alloys.

Half-Heusler alloys have the general chemical formula XYZ and crystallize in the C1b structure, which is derived

✉ H. Baaziz
baaziz_hakim@yahoo.fr

1 Faculty of Technology, University of M'sila, PO Box 166, 28000 IchbiliaM'sila, Algeria

2 Laboratory of Surfaces and Interfaces Studies of Solid Materials, University of Setif 1, Sétif, Algeria

3 Department of Physics, Faculty of Science, University of M'sila, 28000 M'sila, Algeria

4 Laboratory of Physics and Chemistry of Materials, University of M'sila, M'sila, Algeria

5 Department of Basic Education in Technology, Ferhat ABBAS University, Setif 1, Setif, Algeria

6 Faculty of Natural and Life Sciences, Ferhat Abbas Setif 1 University, 19000 Setif, Algeria

7 Faculty of Medicine, University, Ferhat Abbas Setif 1, 19000 Setif, Algeria

Published online: 16 January 2025

from a face-centered cubic (FCC) lattice. In this structure, atoms X, Y, and Z occupy three of the four available FCC sublattices, while the fourth sublattice remains vacant. This unique atomic arrangement influences their electronic and magnetic behavior, making them promising candidates for spintronic and thermoelectric applications. A prominent example of this family is NiMnSb.

Full-Heusler alloys, on the other hand, adopt the chemical formula X_2YZ and crystallize in the $L2_1$ structure [8, 9]. This structure can be viewed as a derivative of the C1b configuration, where the previously vacant site in half-Heusler alloys is now occupied by a second X atom. This additional atomic site results in a more symmetric and dense atomic arrangement, leading to enhanced magnetic and structural stability.

Recently, a third class of Heusler materials has emerged: the quaternary Heusler alloys. These compounds have the general formula XX'YZ, where X and X' are typically transition metals, and Z is often a main group element. Quaternary Heusler alloys combine the structural characteristics of full-Heusler and half-Heusler materials while offering additional tunability in their magnetic and electronic properties. This added complexity and versatility make them particularly attractive for advanced technological applications such as spintronics, optoelectronics, and thermoelectric devices. Notably, these quaternary Heusler alloys exhibit an ordered crystalline structure within the space group $\overline{F}43m$ (No. 216) [10], which contributes to their unique electronic and magnetic properties suitable for various technological applications.

Co-based Quaternary Heusler Alloys (QHAs) have garnered significant attention in research due to their exceptional properties, including high Curie temperatures (T_C), substantial spin polarization, and the ability to tune their electronic structure. Both theoretical studies and experimental findings support these assertions [11, 12].

Experimental investigations have contributed valuable insights into various CoFeMnZ alloys, where Z includes elements like Al, Ga, Si, and Ge. Alijani et al. conducted notable studies in this area [13], focusing on the structural and magnetic properties of these alloys. Basit et al. [14] explored the properties of CoFeTiAl and CoMnVAl alloys, providing further empirical evidence of their potential for applications in spintronics and magnetic devices. Additionally, Enamullah et al. [15] investigated CoFeCrGe, contributing to the expanding knowledge base on Co-based QHAs and their diverse compositions.

These experimental studies complement theoretical investigations by providing crucial empirical data that validate and refine theoretical predictions. Together, they enhance our understanding of Co-based QHAs and pave the way for their utilization in advanced electronic and magnetic technologies. First-principles simulations have revealed that numerous Co-based Quaternary Heusler Alloys (QHAs) exhibit intriguing half-metallic properties, positioning them as promising candidates for applications in spintronics. Noteworthy examples include CoFeMnSi [16], CoFeCrAl [17], CoRuFeSi [18], CoFeTiSi, CoFeTiAs [19], and CoFeTiSb [20]. These materials are characterized by having a unique electronic structure where one spin channel behaves as a metal, while the opposite spin channel exhibits a semiconducting or insulating behavior, leading to a high spin polarization.

In recent studies, Gao et al. synthesized quaternary Heusler alloys CoFeCrZ (Z = Al, Si, Ga, and Ge) and found that CoFeCrAl and CoFeCrSi demonstrate complete half-metallicity [21]. This indicates a 100% spin polarization at equilibrium lattice parameters, a crucial feature for efficient spin injection and manipulation in spintronic devices.

Furthermore, investigations into CoFeZr-based composites, such as CoFeZrGe, CoFeZrSb, and CoFeZrSi, have also demonstrated half-metallic behavior with a spin polarization of 100% under equilibrium conditions [22]. These findings underscore the robustness and potential utility of Co-based QHAs in advancing spintronic technologies, offering enhanced control and efficiency in spin-polarized electronic applications. The exploration of Quaternary Heusler Alloys (QHAs) stands at the forefront of materials research, driven by their potential for revolutionizing diverse technological applications. These alloys, characterized by their unique crystal structures and versatile properties, have garnered significant attention due to their promising attributes in fields ranging from spintronics and magneto-optics to thermoelectrics and beyond. The intricate interplay of their electronic, magnetic, structural, and optical characteristics offers a rich ground for scientific inquiry and practical innovation. In this study, we delve into the theoretical analysis of CoFeYSb (Y = V, Ti) QHAs, employing advanced computational methods to unravel their fundamental properties and explore their potential implications for next-generation electronic and photonic devices. This investigation not only aims to deepen our understanding of these materials at a fundamental level but also seeks to pave the way for their practical applications in cutting-edge technologies.

Building upon our previous research, this study utilizes first-principles calculations to comprehensively analyze the structural, electronic, elastic, optical, and magnetic properties of CoFeYSb alloys, where Y represents either V or Ti. This investigation aims to deepen our understanding of these quaternary Heusler alloys by exploring their multifaceted properties at a fundamental level.

2 Calculation Method

The structural, electronic, magnetic, elastic, and optical properties of CoFeYSb (Y = V, Ti) quaternary Heusler alloys were investigated using density functional theory (DFT) within the pseudopotential plane-wave (PP-PW)

formalism, as implemented in the CASTEP code [23, 24]. The generalized gradient approximation (GGA) with the Perdew-Burke-Ernzerhof (PBE) parameterization [25] was employed to describe the exchange–correlation effects consistently.

The Vanderbilt ultrasoft pseudopotentials were used to model the interaction between core and valence electrons. The considered valence electron configurations are Co: $3d^7\ 4s^2$, Fe: $3d^6\ 4s^2$, V: $3d^3\ 4s^2$, Ti: $3d^2\ 4s^2$, and Sb: $5s^2\ 5p^3$ [26]. A plane-wave cut-off energy of 450 eV was set to ensure accuracy and convergence of the calculations. Brillouin zone integrations were performed using the Monkhorst–Pack scheme [27], with a $12\times12\times12$ mesh for structural optimization and a denser $30\times30\times30$ grid for the calculation of spin-polarized density of states (DOS).

Structural optimization was conducted using the Broyden-Fletcher-Goldfarb-Shanno (BFGS) algorithm [28], with convergence criteria set as follows: total energy tolerance of 5×10^{-6} eV/atom, maximum stress of 0.02 GPa, maximum force of 0.01 eV/Å, and maximum atomic displacement of 0.0005 Å.

The elastic constants (Cij) were calculated using the stress–strain method [29], and the elastic moduli were derived using the Voigt-Reuss-Hill averaging scheme [30–32].

The optical properties were determined on a uniformly distributed k-point grid of $20\times20\times20$. The real and imaginary parts of the dielectric function, ε(ω), were obtained, enabling the calculation of other optical parameters such as absorption coefficient (α(ω)), refractive index (n(ω)), extinction coefficient (k(ω)), energy loss function (L(ω)), reflectivity (R(ω)), and optical conductivity (σ(ω)). These parameters were derived using the following expressions [33]:

$$\alpha(w) = \frac{2kw}{c}$$

$$n(w) = \frac{[|\varepsilon(w)| - \varepsilon_1(w)]^{1/2}}{2}$$

$$k(w) = \left[\frac{|\varepsilon(w)| - \varepsilon_1(w)}{2}\right]^{1/2}$$

$$L(w) = \frac{\varepsilon_2(w)}{\varepsilon_1^2(w) + \varepsilon_2^2(w)}$$

$$R(w) = \frac{(n-1)^2 + k^2}{(n+1)^2 + k^2}$$

$$\sigma(w) = \frac{w}{4\pi}\varepsilon_2(w)$$

3 Results and Discussion

3.1 Structural Aspects

The compound CoFeYSb (where Y = V, Ti) crystallizes in a structure reminiscent of the LiMgPdSn [34] compound or the Y-type quaternary Heusler alloy structure. This structure belongs to the space group $F\bar{4}3m$ (Fig. 1a), characterized by four interpenetrating face-centered cubic sub-lattices. Atoms occupy specific Wyckoff sites within these sub-lattices: 4a (0,0,0), 4c (1/4,1/4,1/4), 4b (1/2,1/2,1/2), and 4d (3/4,3/4,3/4). According to the symmetry of the space group [11, 35–37], there are three distinct non-equivalent substructures classified as YI, YII, and YIII types, as summarized in Table 1. In the YI type substructure, the positions 4a, 4c, 4b, and 4d are occupied by atoms Z, X', Y, and X, respectively. The key distinction between YII (YIII) and YI types lies in the arrangement of atoms Y and X' (or Z and X′). Figure 1

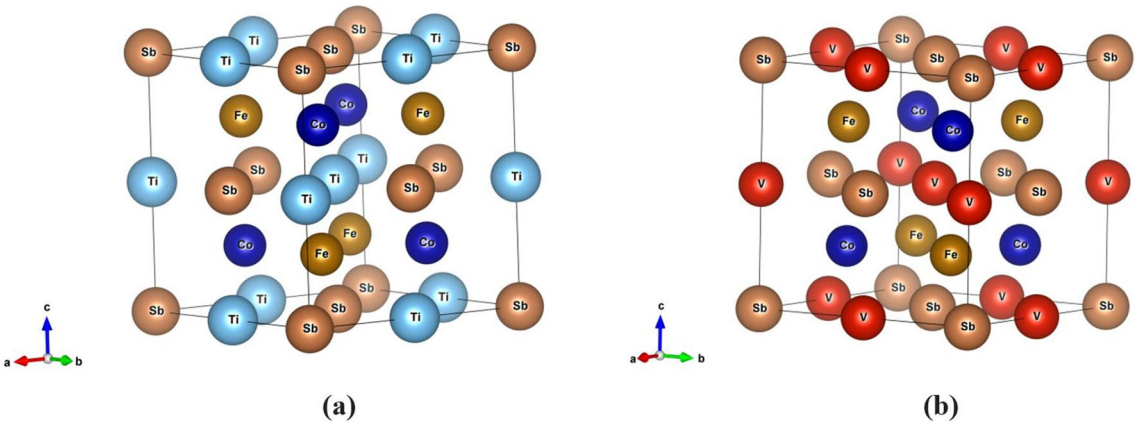

Fig. 1 Crystal structure of Heusler compounds Conventional cell: (**a**) CoFeTiSb (**b**) CoFeVSb

illustrates the YI type substructure of the CoFeYSb (Y = V, Ti) Heusler alloys.

This arrangement and classification provide a structural framework for understanding the atomic positions and symmetries within these compounds, crucial for predicting and interpreting their physical properties and behaviors.

To accurately determine the ground state (refer to Fig. 2), we systematically minimized energy across a range of lattice constants for both ferromagnetic (FM, spin-polarized) and nonmagnetic (NM, non-spin-polarized) configurations. Our findings consistently indicate that the ferromagnetic configuration exhibits greater stability compared to the nonmagnetic configuration. This conclusion is drawn from the observation that the total energy is lower in the ferromagnetic state. Consequently, we proceed to analyze the properties specific to the ferromagnetic configuration below. This configuration serves as the basis for further investigations into the magnetic and electronic properties of the materials studied, providing insights into their potential applications in spintronics, magnetic storage devices, and related fields.Upon careful examination of Fig. 2, it becomes evident that the YI type substructure in its magnetic state achieves the lowest total energy among all configurations considered for CoFeYSb materials (see Fig. 2a and b). This finding strongly suggests that CoFeYSb (Y = V, Ti) Heusler systems are significantly

Table 1 Three different occupying positions of CoFeVSb quaternary Heusler alloys in the Y-Type structures

	4a (0,0,0)	4c (1/4, 1/4, 1/4)	4b (1/2, 1/2, 1/2)	4d (3/4, 3/4, 3/4)
YI	Sb	Fe	Y = V,Ti	Co
YII	Sb	Y = V,Ti	Fe	Co
YIII	Fe	Sb	Y = V,Ti	Co

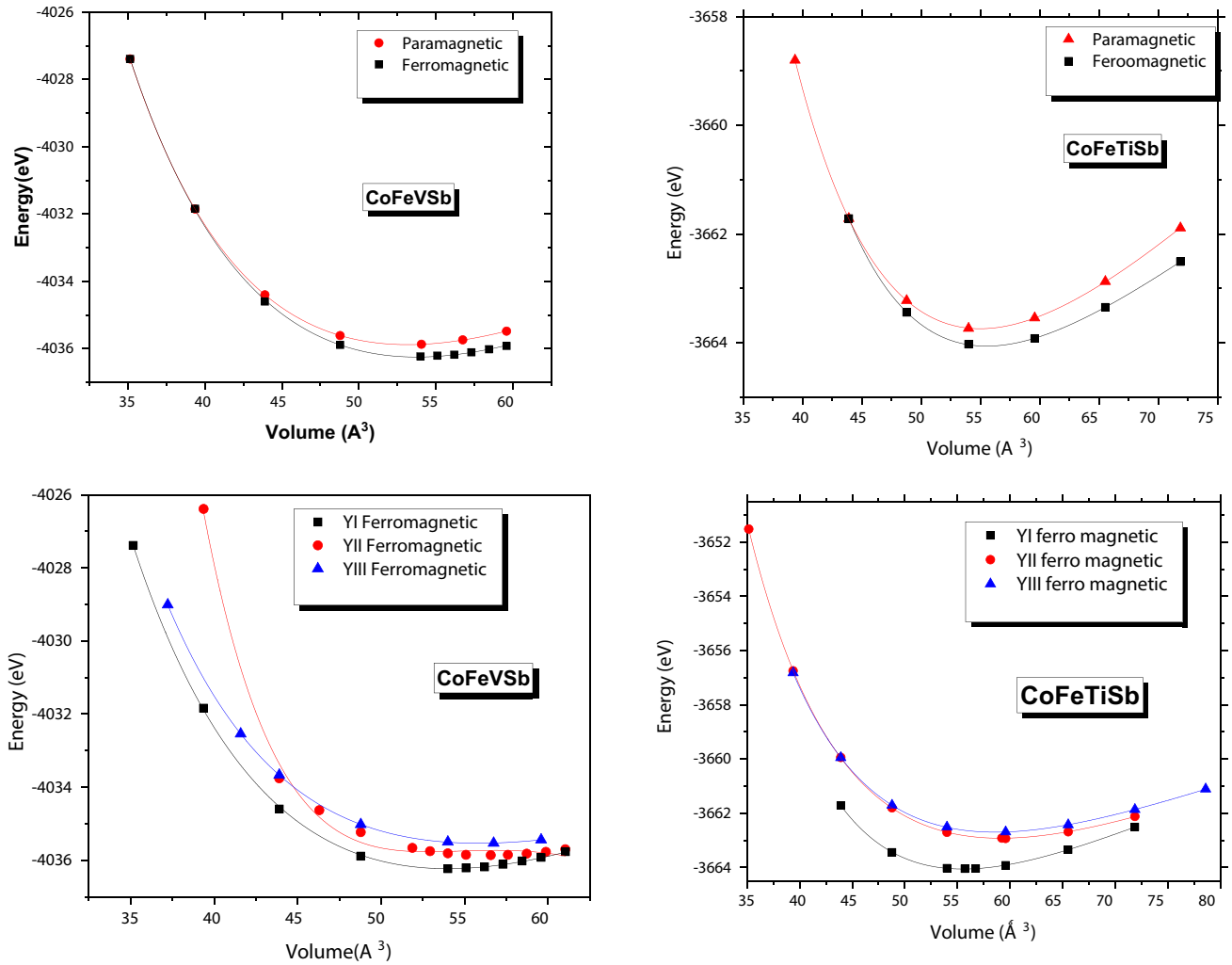

Fig. 2 Total energy vs. unit cell volume for ferromagnetic and paramagnetic configurations of CoFeYSb (Y = V, Ti)

predisposed to crystallize in the YI type substructure over the YII and YIII configurations.

The cohesive and formation energies [37, 38] provide valuable insights into the physicochemical stability of quaternary CoFeYSb (Y = V, Ti) Heusler alloys.

$$E_{coh} = \frac{1}{4}\left[E_{Total}^{CoFeYSb} - (E_{atom}^{Fe} + E_{atom}^{Co} + E_{atom}^{Y} + E_{atom}^{Sb})\right] \quad (1)$$

$$E_{For} = \frac{1}{4}\left[E_{Total}^{CoFeYSb} - (E_{bulk}^{Fe} + E_{bulk}^{Co} + E_{bulk}^{Y} + E_{bulk}^{Sb})\right] \quad (2)$$

The cohesive and formation energies [34, 35] are calculated using the equilibrium total energy $E_{Total}^{CoFeYSb}$, and the equilibrium total energies per atom for bulk Fe, Co, Y (V, Ti), and Sb: $E_{bulk}^{Fe}, E_{bulk}^{Co}, E_{bulk}^{Y}$, and E_{bulk}^{Sb}. Additionally, $E_{atom}^{Fe}, E_{atom}^{Co}, E_{atom}^{Y}$, and E_{atom}^{Sb} represent the isolated atomic energies of Co, Fe, Y (V, Ti), and Sb, respectively. Negative values of these energies indicate the stability of CoFeYSb alloys, suggesting their feasibility for experimental synthesis. These calculations provide essential insights into the physicochemical stability of these compounds, supporting their potential for practical applications in various technological domains.

Table 2 systematically categorizes the structural parameters obtained from our study. Key ground state properties such as the equilibrium lattice constant (a), bulk modulus (B), and its corresponding pressure are meticulously determined by fitting total energies against varied volumes using Murnaghan's equation of state [39]. The findings for both CoFeVSb and CoFeTiSb compounds are in alignment with previously documented results [19, 20], affirming the reliability and consistency of our experimental approach. Notably, an intriguing trend emerges: as the atomic number of element Y increases, there is a discernible reduction observed in the lattice parameter. This trend underscores the systematic influence of atomic composition on the structural characteristics of the compounds under investigation.

3.2 Assessing Elastic Properties

Elastic qualities are critical for accurately assessing a material's mechanical behavior. They go beyond simple parameters like the compressibility modulus B and delve into the intricate details of a solid's elastic stability through elastic constants C_{ij}. These constants are essential macroscopic factors that establish the relationship between applied stress and resulting deformation within homogeneous solids and can be determined using the GGA at zero pressure by the following equation [40, 41]:

$$C_{ij} = \frac{1}{V}\frac{\partial^2 E}{\partial \varepsilon_i \partial \varepsilon_j}$$

While the indices i and j denote both directions of the stresses or strain, and E is the ground state energy.

Understanding these properties offers deep insights into how materials respond to mechanical forces and maintain structural integrity under varying conditions.

The mechanical stability of a cubic system is determined by ensuring that the three independent elastic constants C_{11}, C_{12} and C_{44} satisfy the following Born stability condition [42]:

$$(C_{11} - C_{12}) > 0; (C_{11} + C_{12}) > 0; C_{11} > 0; C_{44} > 0 \text{and} C_{12} < B < C_{11} \quad (3)$$

The elastic constants C_{11}, C_{12}, and C_{44} provide crucial insights into the mechanical behavior of crystals. C_{11} specifically measures the crystal's resistance to unidirectional compression, highlighting its ability to withstand deformation along a single axis. In contrast, C_{12} and C_{44} gauge the material's resistance to shear stress, reflecting its capacity to resist deformation due to forces applied perpendicular and parallel to its crystalline planes, respectively.

In the case of CoFeYSb Heusler materials, where C_{11} exceeds C_{12} and C_{44}, these findings indicate that the material exhibits superior resistance to compression compared to shear stress. This structural characteristic underscores its potential for applications where resistance to compressive forces is critical, such as in structural components subjected to high-pressure environments or in devices requiring robust mechanical stability under load. Understanding these elastic constants provides a foundation for predicting and optimizing the material's performance in various engineering and industrial applications.

Our analysis confirms that CoFeYSb is mechanically stable as it meets the Born stability condition, as illustrated in Table 3. Furthermore, from the computed elastic constants, we derived several key mechanical properties [43] including the bulk modulus B, shear modulus G, Young's modulus E, Poisson's ratio, and anisotropy factor A. These values are comprehensively presented in Table 3.

Table 2 Calculated equilibrium lattice constant (a_0 (Å)), volume (V_0 (Å^3)), bulk modulus (B (GPa), pressure derivative (B'), cohesive energy (E_{coh}) and formation energy (E_{For}) for CoFeYSb (Y = V, Ti) Heuslers alloys

Alloys	a_0 (Å)	V_0 (Å^3)	B_0 (GPa)	B'	E_0 (eV)	E_{coh} (eV/atom)	E_{For} (eV/atom)
CoFeVSb	5.99, 5.99 [17]	54.00	198.01	4.44	−4036.25	- 5.22	−0.03
CoFeTiSb	6,06, 6.06[17], 6.08[18]	55.70	189.99	4.67	−3664.04	−5.58	−0.33

$$B = \frac{C_{11} + 2C_{12}}{3} \tag{4}$$

$$G_V = \frac{C_{11} - C_{12} + 3C_{44}}{5} \tag{5}$$

$$G_R = \frac{5(C_{11} - C_{11})C_{44}}{3(C_{11} - C_{12}) + 4C_{44}} \tag{6}$$

$$G_H = \frac{G_V + G_R}{2} \tag{7}$$

$$E = \frac{9BG}{3B + G} \tag{8}$$

$$A = \frac{2C_{44}}{C_{11} - C_{12}} \tag{9}$$

$$\sigma = \frac{3B - 2G}{2(3B + G)} \tag{10}$$

The compressibility modulus values derived from C_{ij} agree perfectly with those obtained from smoothing the (E-V) state equations. CoFeTiSb exhibits lower resistance to compression (and higher resistance to shear) compared to CoFeVSb, as evidenced by its bulk modulus B = 193 GPa (shear modulus G = 73 GPa), which is less than the bulk modulus of CoFeVSb B = 196 GPa (shear modulus G = 67 GPa). Poisson's ratio (σ) serves to distinguish the nature of interatomic forces within a solid material, indicating that CoFeYSb, with σ approx 0.31, possesses metallic bonding characteristics. Pugh's ratio (B/G), a metric used to distinguish between brittle (B/G < 1.75) and ductile (B/G > 1.75) materials, serves as a valuable indicator of mechanical properties. For CoFeVSb and CoFeTiSb compounds, Pugh's ratio is calculated as 2.92 and 2.63, respectively. These values indicate that both materials exhibit ductile characteristics, given that they surpass the threshold of 1.75.

Table 3 Presently obtained elastic parameters of CoFeYSb (Y = V, Ti)

Parameters	CoFeVSb	CoFeTiSb
C_{11}	252.79	258.62
C_{12}	167.22	160.15
C_{44}	90.50	96.04
B	195.74	192.98
G	67.00	73.45
B/G	2.92	2.63
E	180.41	195.54
σ	0.34	0.33
Θ_D	383.61	405.82
A	0.71	0.56

The Debye temperature (Θ_D), which correlates with both thermal and elastic properties, measures 383.61 K for CoFeVSb and 405.82 K for CoFeTiSb. This parameter provides insights into the materials' thermal conductivity, specific heat capacity, and sound velocity, among other characteristics.

Moreover, the determination of an anisotropy coefficient ($A \neq 1$) reveals that CoFeVSb and CoFeTiSb demonstrate elastic anisotropy. This means that their mechanical properties vary depending on the direction of measurement within the crystal lattice, underscoring the nuanced nature of their elastic behavior.

Together, these parameters provide a comprehensive view of the mechanical and thermal characteristics of CoFeVSb and CoFeTiSb materials, crucial for understanding their potential applications in various technological fields.

To further validate this, an additional assessment was conducted to investigate the three-dimensional (3D) elastic anisotropy behavior of CoFeVSb quaternary Heusler alloys (QHAs). In this context, the term "three-dimensional (3D) closed surfaces" refers to surfaces that illustrate how Young's modulus, E, varies across different crystallographic directions within a cubic crystal [44].

$$\frac{1}{E} = S_{11} - 2\left(S_{11} - S_{12} - \frac{1}{2}S_{44}\right)\left(l_1^2 l_2^2 + l_2^2 l_3^2 + l_3^2 l_1^2\right) \tag{11}$$

where: $S_{ij} = C_{ij}^{-1}$, $l_1 = \sin\theta\cos\varphi$, $l_2 = \sin\theta\sin\varphi$ and $l_3 = \cos\theta$ are the directional cosines concerning the x, y and z axes, respectively. Figures 3(a)-(b) provide visual insights into the three-dimensional closed surfaces depicting the Young's modulus and shear modulus of CoFeYSb (Y = V, Ti) Quaternary Heusler Alloys (QHAs). In isotropic systems, such surfaces exhibit complete spherical geometry in 3D projections. Deviations from this spherical geometry indicate the emergence of elastic anisotropy [45].

The surface analyses of Young's modulus (E) and shear modulus (G) for CoFeYSb (Y = V, Ti) QHAs under 3D projections (Fig. 3(a)-(b)) reveal significant deviations from complete spherical geometry. This observation underscores the distinct elastic anisotropy inherent in CoFeVSb quaternary Heusler alloys (QHAs), as supported by the numerical values presented in Table 3 and corroborated by the findings from the 3D analysis.

To further clarify, these three-dimensional (3D) closed surfaces do not conform to complete spherical geometry. Instead, they depict the nuanced variations in elastic properties across different crystallographic orientations. The plotted cross-sections of these surfaces in various planes, as shown in Fig. 3, demonstrate that Young's modulus and shear modulus exhibits high anisotropy in multiple directions.

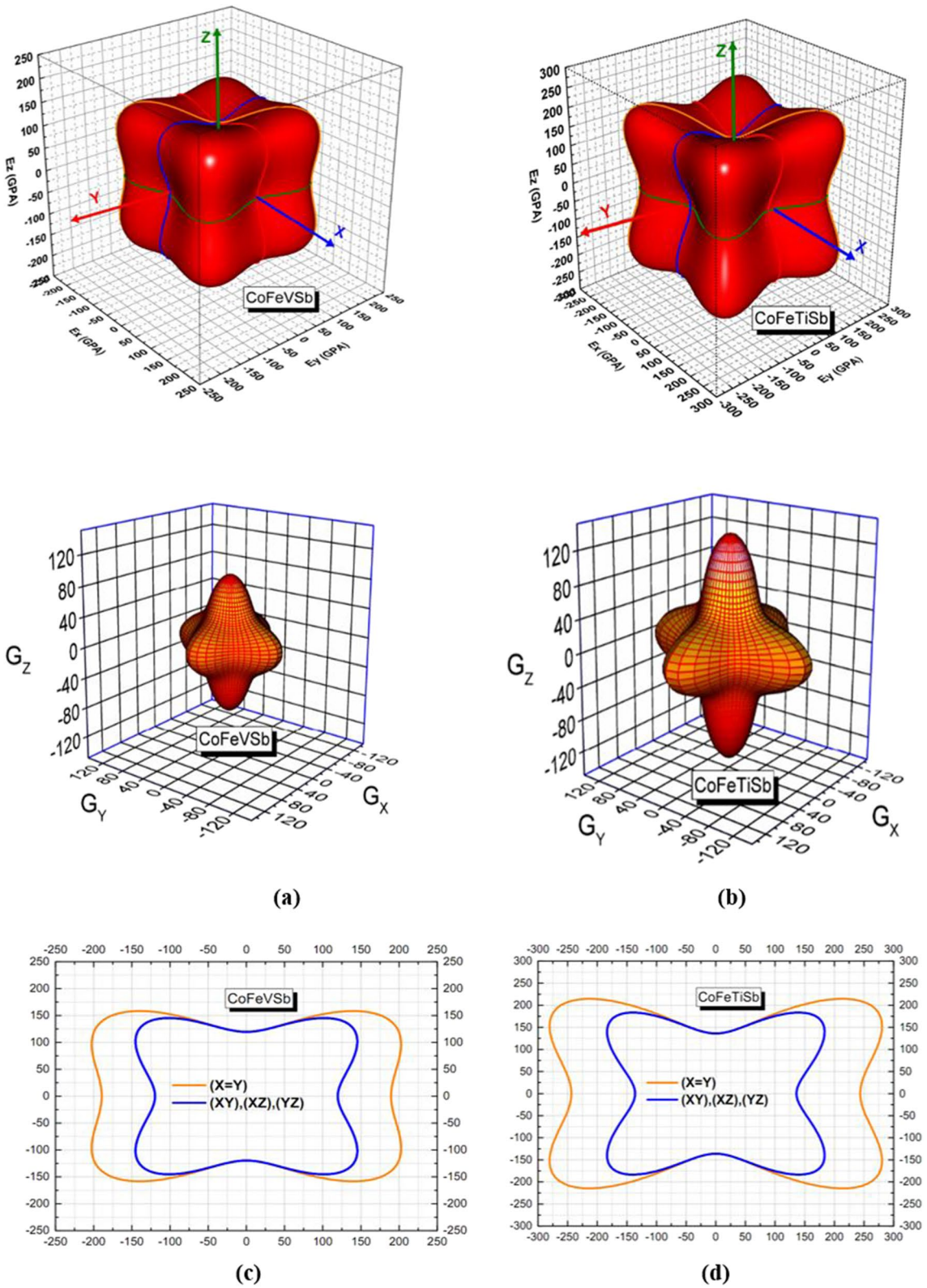

Fig. 3 Graphs of the 3D surface of the Young's modulus and Shear moduli (**a**) CoFeVSb, and (**b**) CoFeTiSb, (**c**), and (**d**), the transverse sections of the Young's modulus in separated planes, respectively

Based on these analyses, it is evident that CoFeTiSb QHAs exhibit a more pronounced anisotropic character compared to CoFeVSb. This distinction in elastic behavior underscores the unique structural and mechanical properties of these materials, which are critical considerations for their potential applications in fields requiring tailored mechanical responses, such as in advanced structural materials and microelectronics.

3.3 Electronic and Magnetic Properties

In Fig. 4, we present the band structure of CoFeYSb compounds, highlighting distinct electronic behaviors for majority (upper panel) and minority spin (bottom panel) electrons. Both CoFeVSb and CoFeTiSb exhibit metallic characteristics near the Fermi level for spin-up states, indicative of conducting behavior. Conversely, the band structures for spin-down states reveal semiconductor properties, with respective band gaps of 0.55 eV and 0.61 eV for CoFeVSb and CoFeTiSb (see Table 4). These band gaps are observed to be indirect, occurring between the Γ and X points within the reciprocal body-centered cubic (bcc) unit cell. The band structure of CoFeYSb compounds is composed primarily of four sp states located at lower energies—comprising one s state and three p states. Additionally, higher energy levels are populated by eight states arising from the hybridization of d orbitals of transition metals. These electronic configurations contribute to the diverse electronic and magnetic properties observed in these quaternary Heusler alloys. This detailed analysis of the band structures provides critical insights into the fundamental electronic properties of CoFeYSb compounds, crucial for understanding their potential applications in electronic and spintronic devices. Among these eight states, the triple t_{1u} states located just in below the Fermi level followed by the triple states t_{2g} and double e_g. The energy gap in the spin-down band is between the occupied t_{1u} states and the e_u states unoccupied with values equal to 0.55 and 0.61 eV for the compounds CoFeVSb, CoFeTiSb, respectively.

Figure 5 illustrates the total (TDOS) and partial (PDOS) densities of states for the quaternary Heusler compounds CoFeYSb. These compounds exhibit metallic behavior for a spin orientation direction (spin-up) and semiconductor behavior for the other direction (spins-down). They are then half-metallic and exhibit a spin polarization of 100% at the Fermi level (see Table 4). From this figure, we note also a strong hybridization between the 3d states of the Co, Fe and Y atoms with a small contribution from the s and p states of the Sb atom. We also notice that the total state density of each atom is essentially formed from the 3d states of the elements Co, Fe and Y.

Figure 6 represents the hybridization between the d orbitals of transition metal atoms. We first consider the Co-Fe interactions, Fe hybridize strongly creating 5 bonding states (e_g doubly degenerate and t_{2g} triply degenerate) which obey tetrahedral symmetry and 5 antibonding states (e_u doubly degenerate and t_{1u} triply degenerate) of octahedral symmetry. The states e_g and t_{2g} hybridize in turn with the d orbitals of the Y atom of the same symmetry giving birth of five bonding states (e_g and t_{2g}) and five antibonding states (e_u and t_{1u}). The e_u and t_{1u} states, of octahedral symmetry, resulting from Co-Fe hybridization cannot hybridize with orbitals d Y atoms of tetrahedral symmetry and then remain non-binding states. Thus, a gap appears in the minority spin band whose width is determined by the interaction Co-Fe. CoFeTiSb compounds have 26 valence electrons per unit cell, 9 for Co, 8 for Fe, 4 for Ti and 5 for Sb. From band structures, 12 electrons occupy the spin-down bands (1 s band of the Sb atom, 3 p bands of the Sb atom and eight bands coming from the hybridization of the d orbitals of transition metals, and the 14 electrons are located in the spin-up bands. The remaining one electron of 27ones in CoFeVSb partially occupies the two spin-up bands around the Fermi level, which comes from the V and Fe 3d states with little contribution of Co 3d states.

The investigation into CoFeYSb (Y = V, Ti) Quaternary Heusler Alloys (QHAs) encompasses a thorough analysis of their magnetic properties, crucial for understanding their potential applications in spintronics and magnetic storage technologies. The total and partial magnetic moments of CoFeYSb were determined through Hirshfeld electron population analysis, as summarized in Table 3. Notably, the predominant contribution to the total magnetic moment of these alloys stems from the Fe and Co atoms, underscoring their pivotal role in the magnetic behavior of the QHAs.

For the CoFeVSb and CoFeTiSb Heusler compounds, the calculated total magnetic moments M_{TOT} are 3 μ_B and 2 μ_B, respectively, at ambient pressure (0 GPa). These results closely adhere to the predictions of the Slater-Pauling law, which states that the total magnetic moment M_{TOT} for Heusler alloys can be expressed as $M_{TOT} = (Z_{TOT} - 24)\,\mu_\beta$, where Z_{TOT} is the total number of valence electrons [46, 47]. Specifically, for CoFeVSb, the total number of valence electrons is 26 (Co: 9, Fe: 8, V: 5, Sb: 4), yielding a predicted magnetic moment of 3 μ_B,

Table 4 The calculated magnetic moments, m(Tot), m(Fe), m(Y), m(Co), m(Sb) in μ_B, Band gap (E_g) in eV, and polarization *P* in %

Alloys	m(Co)	m(Fe)	m(Y)	m(Sb)	M(Tot)	E_g	*P*
CoFeVSb	1.09	1.12	0.75	0.03	2.99	0.55	100%
CoFeTiSb	1.03	1.16	−0.20	0.01	2.00	0.61	100%

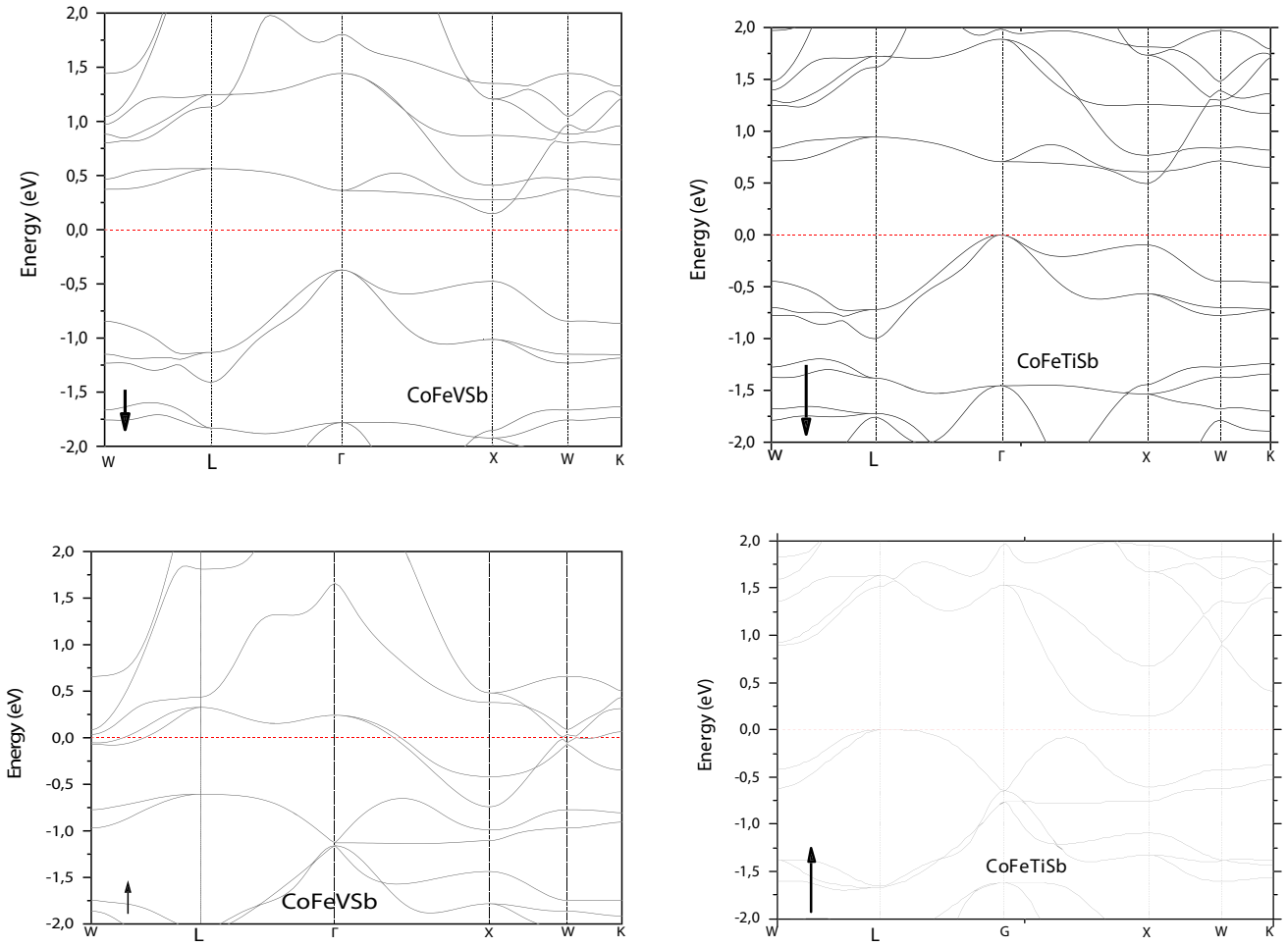

Fig. 4 Spin polarized band structure of CoFeYSb (Y = V, Ti) at their equilibrium lattice

which is in excellent agreement with our calculated value. Similarly, for CoFeTiSb, with 25 valence electrons, the predicted magnetic moment is 2 μ_B (see Table 4), which matches our computed result. This close alignment indicates that the materials obey the general trend outlined by the Slater-Pauling law, further validating the accuracy and consistency of our computational methodology.

Moreover, the calculated magnetic moment values of these compounds are in very good agreement with prior theoretical studies, such as those reported by [19] and [20], which support the robustness of our approach. These previous studies also found similar magnetic moment values for CoFeVSb and CoFeTiSb, reinforcing the reliability of the calculations presented in this work. The consistency with the Slater-Pauling rule confirms that our theoretical framework is reliable for predicting magnetic properties in Heusler alloys.

The agreement with experimental data and the Slater-Pauling law demonstrates the robustness of our computational approach, highlighting its predictive power in assessing the magnetic behavior of these materials. It also underscores the potential of CoFeYSb (Y = V, Ti) Heusler alloys for magnetic and spintronic applications, where precise control over magnetic moments is crucial for optimizing performance.

In conclusion, our analysis of the magnetic moments in CoFeYSb (Y = V, Ti) Heusler alloys contributes to a deeper understanding of their magnetic properties. The consistency with the Slater-Pauling law and prior theoretical studies not only strengthens the validity of our computational approach but also indicates the materials' promising potential for future technological applications. These findings pave the way for further exploration of CoFeYSb quaternary Heusler alloys, focusing on their optimization for next-generation electronic and magnetic devices.

3.4 Optical Behavior and Related Features

In our exploration of Quaternary Heusler Alloys (QHAs), understanding their optical properties is crucial for assessing

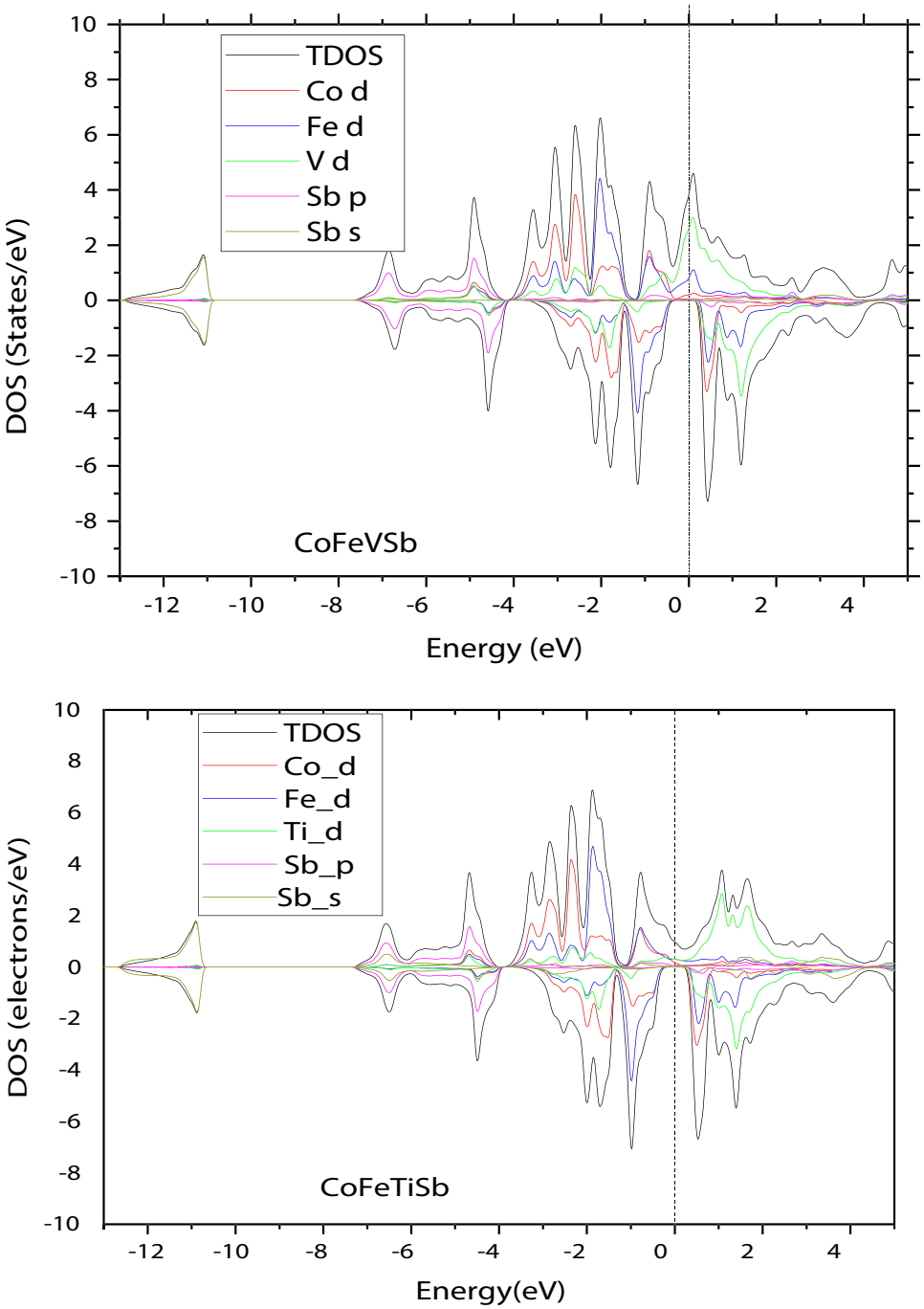

Fig. 5 The total and partial density of states of the CoFeYSb (Y = V, Ti) in type 1 calculated by GGA

their potential in various optoelectronic applications. The analysis involved a comprehensive examination of how these materials interact with electromagnetic radiation across a spectrum of frequencies. By calculating complex dielectric constants, refractive indices, absorption coefficients, and related optical parameters as functions of the complex frequency (ω), we gained valuable insights into their optical behavior. These findings not only deepen our theoretical understanding but also provide practical implications for designing devices that utilize light-matter interactions. For a detailed visualization and comprehensive data set, please refer to Fig. 7, which illustrates the outcomes of our optical property analysis for the studied QHAs. At high frequencies, the complex dielectric constants ε(ω) consist of two components: the real part, represented by the dielectric function $\varepsilon_1(\omega)$, and the imaginary part, represented by the dielectric function $\varepsilon_2(\omega)$ [48]: $\varepsilon(\omega) = \varepsilon_1(\omega) + i\varepsilon_1(\omega)$. The $\varepsilon_1(\omega)$ parameter generally quantifies the level of material polarisation [see to Fig. 7(a)]. The computed static real dielectric constants $\varepsilon_1(0)$ for CoFeVSb and CoFeTiSb are

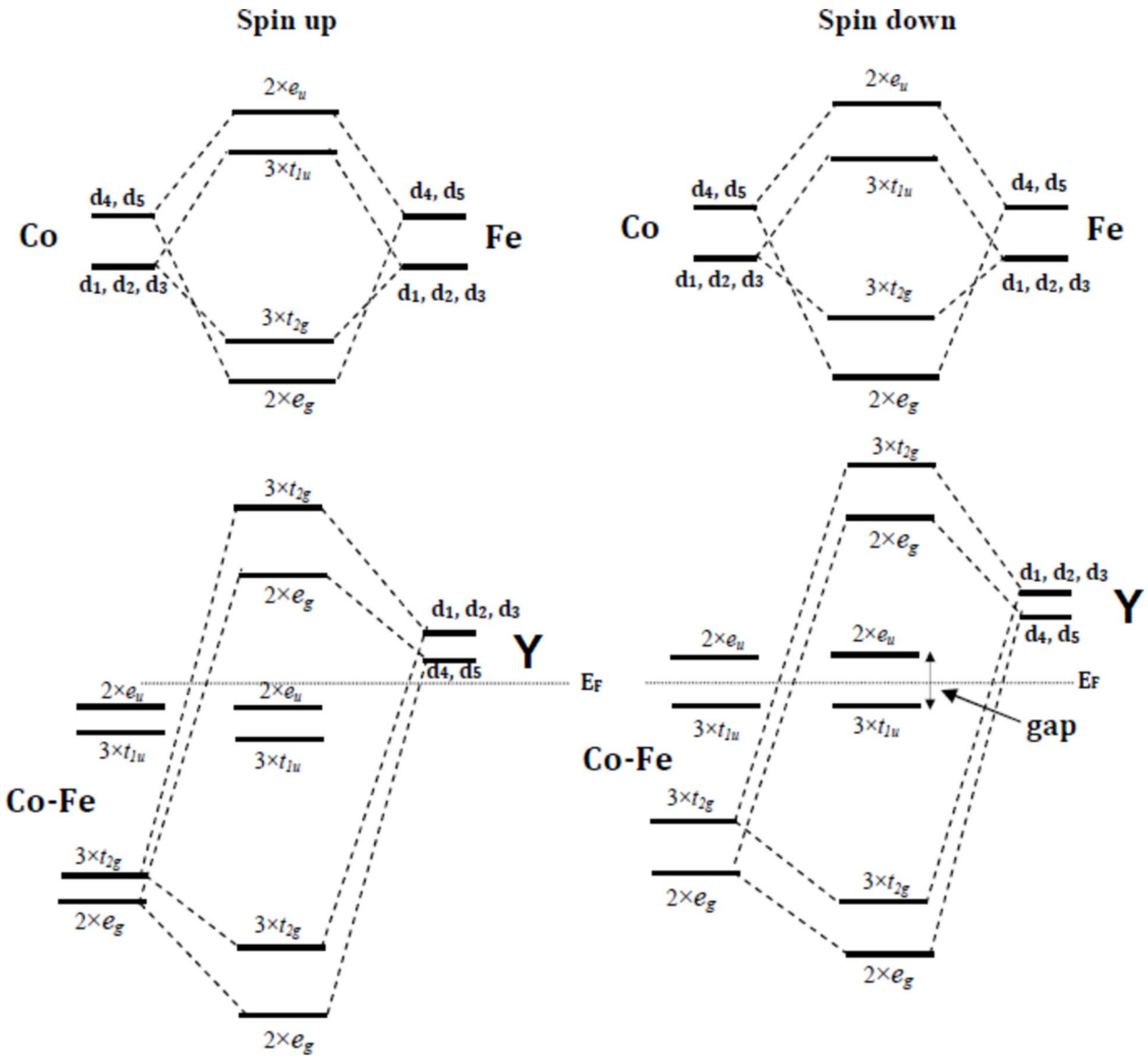

Fig. 6 Diagram depicting the majority–minority gap's origins in CoFeYSb (Y = V, Ti)

127.61, and 50.05, respectively. The occurrence of a negative value of ε_1 in the higher photon energy range (for CoFeVSb and CoFeTiSb, negative ε_1 values appear when $\omega > 2.55$ eV, and 3.01 eV respectively) is responsible for the attenuation of light propagation, mostly caused by plasmon oscillations [49]. The ε_2 (ω) is closely linked to the extinction coefficient and optical absorption, and it represents the interband transition between the valence band and conduction band. Examining Fig. 7(a), it is evident that the highest peaks of ε_2, which fall between the energy range of 0.49 eV to 2.04 eV, for CoFeVSb and CoFeTiSb, respectively. The minimum threshold energy values obtained, 0.48 eV for CoFeVSb and 0.58 eV for CoFeTiSb, align closely with their respective optical band gaps. These optical band gaps signify the energy required for the first electron transition from the highest energy level in the valence band to the lowest energy level in the conduction band along the Γ-X symmetry direction.

Even at $\omega = 0$ eV, the values of ε_2 (the imaginary part of the dielectric function) for CoFeVSb and CoFeTiSb are approximately 31.08 and 4.64 arbitrary units, respectively. This suggests that both materials exhibit non-zero absorption coefficients at zero photon energy, indicating inherent electronic transitions or excitations.

Moreover, the peaks in the optical absorption spectra for CoFeVSb and CoFeTiSb are observed at energies approximately 0.44 eV and 2.04 eV, respectively. These peaks correspond to specific photon energies where there is a significant increase in the absorption coefficient, highlighting the materials' ability to absorb light in these energy ranges.

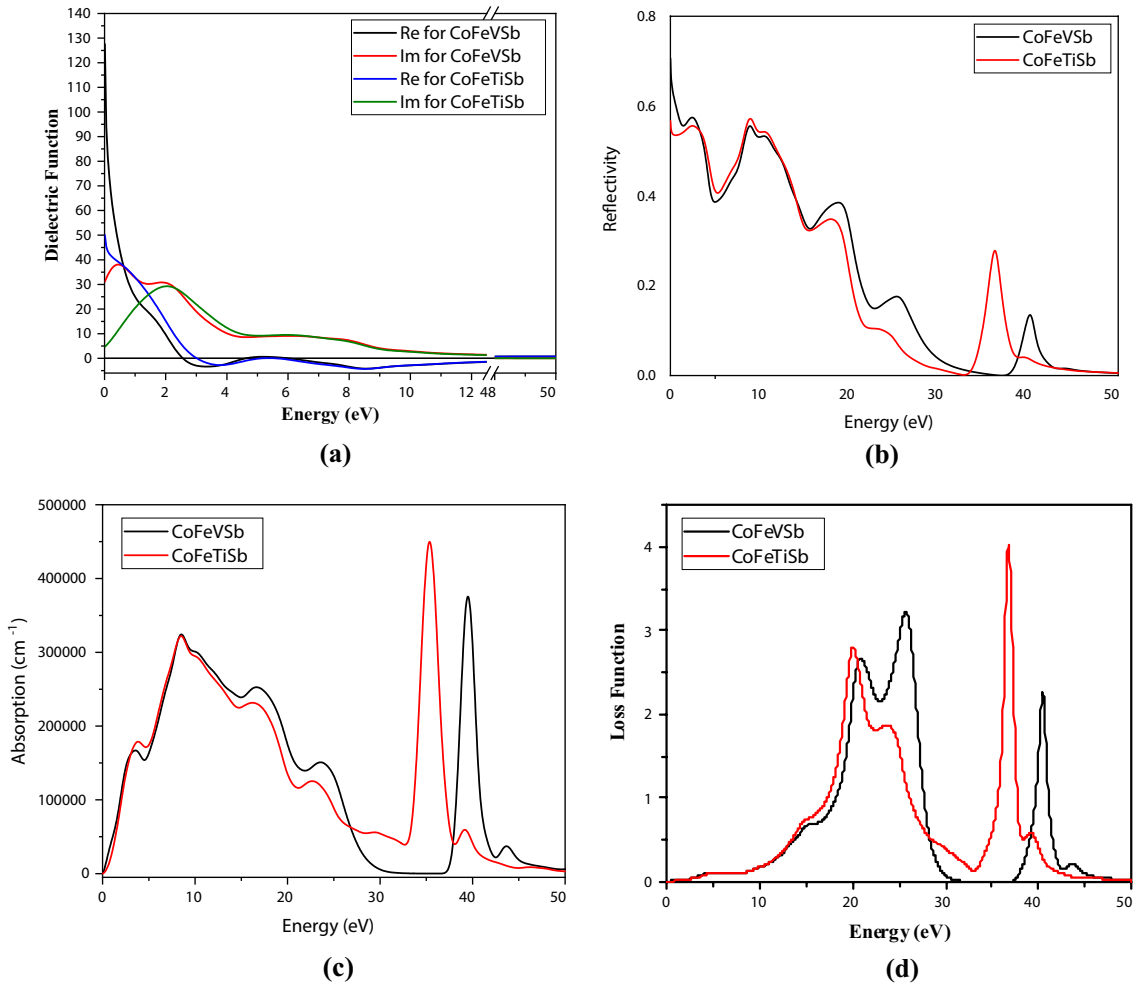

Fig. 7 (**a**) Dielectric function (**b**) Reflectivity spectra and (**c**) absorption coefficient and (**d**) the energy loss L(w) as a function of energy for CoFeYSb (Y = V, Ti) with GGA

These findings underscore the potential of CoFeVSb and CoFeTiSb compounds for optoelectronic applications, as their optical properties align with requirements for devices such as photodetectors, solar cells, and light-emitting diodes (LEDs). Understanding these optical characteristics provides crucial insights into how these materials can be tailored and utilized in advanced technologies reliant on photon absorption and emission processes.

The investigation of optical properties aims to provide a comprehensive understanding of reflectivity and optical absorption, as illustrated in Fig. 7(b) and (c). The reflectivity spectra reveal that both compounds exhibit similar characteristics in the higher photon energy region. Specifically, at a photon energy of $\omega = 0$ eV, the reflectivity values for CoFeVSb and CoFeTiSb are measured at 65% and 0.56%, respectively. In the ultraviolet (UV) range, spanning from 6.5 eV to 13 eV, both materials demonstrate a reflectivity of approximately 44%. This indicates that CoFeVSb and CoFeTiSb possess considerable potential as effective shields against ultraviolet radiation. Such UV shielding capabilities are highly desirable for applications in protective coatings, optical filters, and devices where mitigation of UV exposure is critical for material longevity and human safety.Understanding these reflectivity characteristics not only informs their potential use in UV protection but also contributes to the broader utilization of these compounds in optical and photonic applications, where precise control over light reflection and absorption is essential. Based on Fig. 7(c), it can be observed that the absorption coefficient curve, which represents the relationship between photon energy and absorption, is consistent with other optical properties such as ε_2. Specifically, there is a significant rise in absorption between photon energies of 0–30 eV, and 33–40 eV. For CoFeVSb and CoFeTiSb compounds, our investigation reveals significant optical absorption characteristics across a range of energies. Initially, optical absorption begins at approximately 0.01 eV, positioning it within the infrared

(IR) spectrum. Remarkably, even at ω = 0 eV, both materials exhibit a non-zero absorption coefficient.

Furthermore, our data indicates a notable enhancement in optical absorption as the element Y transitions from Ti to V, particularly evident above ω = 30 eV. The most pronounced optical absorption peaks occur in the visible to ultraviolet (Vis-UV) range, where the absorption coefficient exceeds 10^5 cm^{-1}. This finding suggests that CoFeVSb and CoFeTiSb compounds hold promise for applications in optoelectronic devices [50–57].

By leveraging these enhanced optical absorption properties, these materials could potentially contribute to the development of efficient photovoltaic cells, sensors, and other devices requiring high sensitivity to light across a broad spectrum. These characteristics underscore their suitability and potential in advancing technologies reliant on optical interactions.

The electron energy loss function (EELF) provides crucial insights into the energy dissipation processes when high-energy electrons interact with a material. Peaks observed in the EELF spectrum, particularly in the L(ω) spectrum, are known as plasmon peaks and denote collective electron oscillations within the substance.

In our study, as depicted in Fig. 7(d), the energy loss spectra of CoFeVSb and CoFeTiSb compounds exhibit distinct peaks within specific energy ranges. For CoFeVSb, notable peaks are observed in the energy range of 17–27 eV. Specifically, the peak energy identified is 25.86 eV. On the other hand, CoFeTiSb shows prominent peaks in the higher energy range of 35–40 eV, with a peak energy measured at 36.71 eV.

These observed plasmon peaks are indicative of the materials' electronic structure and their ability to support collective electron oscillations at these characteristic energies. Understanding these features is critical for applications involving electron energy loss spectroscopy (EELS), such as in the fields of materials science, surface science, and nanotechnology, where precise knowledge of energy dissipation mechanisms is essential.

The optical properties of CoFeYSb (Y = V, Ti) Heusler alloys have been extensively examined, with a particular focus on their potential applications in optoelectronic systems. The weak reflectivity of these materials across the visible and near-infrared regions is a critical feature that enhances their absorption of incident photons, a key factor for optoelectronic devices such as photodetectors and solar cells. In addition to the low reflectivity, the alloys exhibit excellent optical conductivity, further underscoring their suitability for applications that require efficient interaction with light.

The optical conductivity of these alloys shows a broad absorption spectrum, which is indicative of their ability to absorb a wide range of photon energies. This characteristic is particularly important for optoelectronic applications such as thin-film solar cells, where maximizing photon absorption across a broad spectrum is crucial for enhancing device efficiency. The strong absorption of energetic photons in the UV–visible spectrum, coupled with the high optical conductivity, suggests that these alloys could function effectively as materials for light-harvesting applications, especially in devices designed to operate under different lighting conditions.

Moreover, the alloys' weak reflectivity makes them suitable for minimizing energy losses, a significant advantage in optoelectronic systems. The ability to efficiently absorb light while maintaining high conductivity enables these alloys to be used in a variety of optoelectronic devices that require robust, energy-efficient materials.

Recent studies (e.g., [33, 58]) have demonstrated the advantages of using Heusler alloys in optoelectronic applications due to their favorable electronic and optical properties. These findings align with our results, further validating the suitability of CoFeYSb Heusler alloys for next-generation optoelectronic devices. Specifically, the low reflectivity and high absorption of these materials suggest they could be key components in photovoltaic technologies, particularly in thin-film solar cells, where light absorption and charge transport are critical for high efficiency.

In summary, the CoFeYSb (Y = V, Ti) Heusler alloys display remarkable optical properties, including weak reflectivity, excellent optical conductivity, and high photon absorption. These attributes, combined with their other material characteristics, make them strong candidates for emerging optoelectronic applications. The findings from this study highlight the potential for these materials in advancing technologies such as solar cells, photodetectors, and other optoelectronic systems, paving the way for future research and optimization in this area.

4 Conclusion

In this study, we investigated the magnetic, mechanical, electronic, optical, and anisotropic properties of CoFeYSb (Y = V, Ti) quaternary Heusler alloys (QHAs) using first-principles calculations. The key findings of this study can be summarized as follows:

- Geometry optimizations confirmed the chemical stability of CoFeVSb and CoFeTiSb Heusler alloys, with a preference for the ferromagnetic (or ferrimagnetic) YI-type structure.
- The elastic constants (Cij) of CoFeYSb alloys (Y = V, Ti) highlighted their mechanical stability, ductility, and anisotropic behavior. These alloys showed stronger

resistance to uniaxial strain compared to shear deformation.

- Electronic structure analyses revealed the half-metallic nature of CoFeYSb alloys, exhibiting high spin polarization (100%) and a noticeable energy gap in the minority spin channel. The total magnetic moments of CoFeVSb and CoFeTiSb were in agreement with the Slater-Pauling rule, indicating their suitability for spintronic applications.
- The optical properties, including the dielectric function, absorption coefficient, and energy loss function, demonstrate that CoFeYSb alloys exhibit significant absorption in the visible and ultraviolet ranges. These characteristics suggest their potential for use in optoelectronic devices. Consequently, CoFeYSb alloys may serve as excellent optical conductors in practical applications across the visible and ultraviolet spectrum.

In conclusion, both CoFeVSb and CoFeTiSb Heusler alloys show great promise for future spintronic and optoelectronic applications due to their unique combination of magnetic and optical properties.

Acknowledgements The authors would like to express gratitude to the General Directorate for Scientific Research and Technological Development for the financial assistance they provided over the course of this work's execution.

Author Contribution I. Bensehil, Writing- Original draft preparation, review & editing, H. Baaziz, Supervision; Methodology, review & editing , Z.Charifi, Writing—original draft, Writing – review & editing T. Ghellab, Data curation, Formal analysis, F. Djeghloul Investigation, Methodology, S. Zaiou review & editing, A. Kolli Data curation, Formal analysis, review & editing, N. Guechi review & editing,

Data Availability No datasets were generated or analysed during the current study.

Declarations

Competing Interests The authors declare no competing interests.

References

1. Barla, P., Joshi, V.K., Bhat, S.: J. Comput. Electron.Comput. Electron. **20**, 805–837 (2021)
2. Žutić, I., Fabian, J., DasSarma, S.: Rev. Modern. Phys. **76**, 323 (2004)
3. Katsnelson, M., Irkhin, V.Y., Chioncel, L., Lichtenstein, A., de Groot, R.A.: Rev. Mod. Phys. **80**, 315 (2008)
4. Hussain, M.K., Abdulsadah, F.H., Ali, M.M.: Mater. Today: Proc. **18**, 2590–2594 (2019). https://doi.org/10.1016/j.matpr.2019.07.117
5. Hussain, M.K., Yao, Kl.: Appl. Phys. A **125**, 463 (2019). https://doi.org/10.1007/s00339-019-2752-0
6. de Groot, R.A., Mueller, F.M., van Engen, P.G., Buschow, K.H.J.: Phys. Rev. Lett. **1983**, 50 (2024)
7. de Groot, R.A., Buschow, K.H.J.: J. Magn. Magn. Mater. **54–57**, 1377 (1986)
8. Galanakis, I.: Springer. Ser. Mater. Sci. 3–36 (2015)
9. Felser, C., Wollmann, L., Chadov, S., Fecher, G.H., Parkin, S.S.P.: Springer. Ser. Mater. Sci. 37–48 (2015)
10. Wurmehl, S., Wójcik, M., Springer. Ser. Mater. Sci. 87–109 (2015)
11. Nag, J., Rani, D., Singh, D., Venkatesh, R., Sahni, B., Yadav, A., Jha, S., Bhattacharyya, D., Babu, P., Suresh, K.: Phys. Rev. B **105**, 144409 (2022)
12. Mouatassime, M., Selmani, Y., Idrissi, S., Bahmad, L., Goumrhar, F., Labrim, H., Benyoussef, A.: J. Solid State Chem. **304**, 122534 (2021)
13. Vajiheh, A., et al.: Phys. Rev. B **84**, 224416 (2011)
14. Basit, L., Fecher, G.H., Chadov, S., Balke, B., Felser, C.: Eur. J. Inorg. Chem. 3950 (2011)
15. Enamullah, Y., Venkateswara, S., Gupta, Varma, M.R., Singh, P., Suresh, K.G., Alam, A.: Phys. Rev. B. **92**, 224413 (2015)
16. Bainsla, L., Mallick, A.I., Raja, M.M. Nigam, A.K., Varaprasad, B.C.S., Takahashi, Y.K., Aftab Alam, K.G., Suresh, K.H., Phys. Rev. B. **91**, 104408 (2015)
17. Tsuchiya, T., Roy, T., Elphick, K., Okabayashi, J., Bainsla, L., Ichinose, T., Suzuki, K.Z., Tsujikawa, M., Shirai, M., Hirohata, A., Mizukami, S.: Phys. Rev. Mater. **3**, 084403 (2019)
18. Bainsla, L., Suresh, K.G.: Appl. Phys. Rev. **3**, 031101 (2016)
19. Xiong, L., et al.: J. Magn. Magn. Mater. **360**, 98–103 (2014)
20. Berri, S., et al.: J. Magn. Magn. Mater. **354**, 65–69 (2014)
21. Gao, G.Y., Hu, L., Yao, K.L., Luo, B., Liu, N.: J. Alloy. Compd. **551**, 539 (2013)
22. Paudel, R., Zhu, J.: J. Magn. Magn. Mater. **453**, 10–16 (2018)
23. Segall, M.D., Lindan, P.J.D., Probert, M.J., Pickard, C.J., Hasnip, P.J., Clark, S.J., Payne, M.C.: First-principles simulation: ideas, illustrations and the CASTEP code. J. Phys. Condens. Matter **14**, 2717–2744 (2002)
24. Clark, S.J., Segall, M.D., Pickard, C.J., Hasnip, P.J., Probert, M.I.J., Refson, K., Payne, M.C.: First principles methods using CASTEP. Z. Kristallogr. **220**, 567–570 (2005). https://doi.org/10.1524/zkri.220.5.567.65075
25. Perdew, J.P., Burke, K., Ernzerhof, M.: Generalized gradient approximation made simple. Phys. Rev. Lett. **77**, 3865–3868 (1996). https://doi.org/10.1103/PhysRevLett.77.3865
26. Vanderbilt, D.: Soft self-consistent pseudopotentials in a generalized eigenvalue formalism. Phys. Rev. B **41**, 7892–7895 (1990). https://doi.org/10.1103/.41.7892
27. Monkhorst, H.J., Pack, J.D.: Phys. Rev. B **13**, 5188 (1976)
28. Fischer, T.H., Almlof, J.: J. Phys. Chem. **96**, 9768 (1992)
29. Nye, J.F.: Physical Properties of Crystals: Their Representation by Tensors and Matrices. Oxford University Press, Oxford (1985)
30. Voigt, W.: Lehrbuch der Kristallphysik. Teubner, Leipzig (1928)
31. Reuß, A.: Angew. Math. Mech. **9**, 49 (1929)
32. Hill, R.: Proc. Phys. Soc. A **65**, 349 (1952)
33. Hussain, M.K., Kahdum, B.J., Paudel, R., S.: Syrotyuk. Electron. Mater **52**, 258–269 (2023). https://doi.org/10.1007/s11664-022-09981-1
34. Drews, J., Eberz, U., Schuster, H.-U.: Optische Untersuchungen an farbigen Intermetallischen phasen. Journal of The Less-Common Metals. **116**(1), 271–278 (1986). https://doi.org/10.1016/0022-5088(86)90235-3
35. Venkateswara, Y., Gupta, S., Varma, M.R., Singh, P., Suresh, K.G., Alam, A.: Electronic structure, magnetism, and antisite disorder in CoFeCrGe and CoMnCrAl quaternary Heusler alloys. Phys. Rev. B **92**, 1–7 (2015). https://doi.org/10.1103/92.224413.224413
36. Bensehil, I., Baaziz, H., Ghellab, T., Charifi, Z., Kolli, A., Guechi, N.: Phys. Stat. Solidi. B. **260**(9), 2300178.

37. Kolli, A., Guechi, N., Kharoubi, M., Kharmouche, A.: Physica B **673**, 415498 (2024)
38. Seh, A.Q., Gupta, D.C.: J. Alloys Compd. **871**, 159560 (2021)
39. Murnaghan, F.D.: Proc. Natl. Acad. Sci. U.S.A. **30**, 244 (1944)
40. Hussain, M.K., Ahmed, A.N.: Optik **226**, 165948 (2021). https://doi.org/10.1016/j.ijleo.2020.165948
41. Kittel, C.: Physique de L'état Solide. Ed. (1996)
42. Born, M., Huang, K.: Dynamical Theory of Crystal Lattices. Clarendon, Oxford (1956)
43. Jamal, M., Jalali Asadabadi, S., Ahmad, I., Rahnamaye Aliabad, H.A.: Comput. Mater. Sci. **95**, 592 (2014)
44. Liao, M., Liu, Y., Min, L., Lai, Z., Han, T., Yang, D., Zhu, J.: Intermetallics **101**, 152–164 (2018)
45. Nye, J.F.: Properties of Crystals. Oxford University Press, New York (1985)
46. Ozdogan, K., Şaşıoğlu, E., Galanakis, I.: J. Appl. Phys. **113**, 193903 (2013)
47. Alijani, V., Winterlik, J., Fecher, G.H., Naghavi, S.S., Felser, C.: Phys. Rev. B **83**, 184428 (2011)
48. Ambrosch-Draxl, C., Sofo, J.O.: Comput. Phys. Commun. 1751 (2006)
49. Zosiamliana, R., Lalrinkima, N., Chettri, B., Abdurakhmanov, G., Ghimire, M.P., Rai, D.P.: RSC. Adv. 1212453 (2022)
50. Ghellab, T., Baaziz, H., Charifi, Z., Telfah, M., Alsaad, A., Telfah, A., Hergenroder, R., Sabirianov, R.: Mater. Sci. Semicond. Process. **141**, 106415 (2022)
51. Ghellab, T., Baaziz, H., Charifi, Z., Bouferrache, K., Saeed, M.A., Telfah, A.: Mater. Res. Express **6**, 075906 (2019)
52. Ghellab, T., Baaziz, H., Charifi, Z., Bouferrache, K., Uğur, Ş, Uğurand, G., Ünver, H.: Int. J. Mod. Phys. B **33**, 1950234 (2019)
53. Mili, I., Latelli, H., Ghellab, T., Charifi, Z., Baaziz, H., Soyalp, F.: Int. J. Mod. Phys. B **35**(7), 2150100 (2021)
54. Telfah, A., Ghellab, T., Baaziz, H., Charifi, Z., Alsaad, A.M., Sabirianov, R.: J. Magn. Magn. Mater. **562**, 169822 (2022)
55. Charifi, Z., Ghellab, T., Baaziz, H., Soyalp, F.: Int. J. Energy Res. **46**(10), 13855–13873 (2022). https://doi.org/10.1002/er.8104
56. Ghellab, T., Baaziz, H., Charifi, Z., Latelli, H.: Physica B **653**, 414678 (2023). https://doi.org/10.1016/j.physb.2023.414678
57. Mekki, H., Baaziz, H., Charifi, Z., Ghellab, T., Genç, A.E., Uğur, Ş, Uğur, G.: Solid State Commun. **363**, 115103 (2023). https://doi.org/10.1016/j.ssc.2023.11
58. Hussain, M.K., Paudel, R., Kahdum, B.J., Syrotyuk, S.: Mater. Chem. Phys. **327**, 129778 (2024)